



Fluorine-doped carbon quantum dot interfacial layer on stockade-like etched copper foil for boosting Li-ion storage

Dong-Yo Shin^a, Ki-Wook Sung^b, Hyo-Jin Ahn^{a,b,*}

^a Program of Materials Science & Engineering, Convergence Institute of Biomedical Engineering and Biomaterials, Seoul National University of Science and Technology, Seoul 01811, Republic of Korea

^b Department of Materials Science and Engineering, Seoul National University of Science and Technology, Seoul 01811, Republic of Korea

ARTICLE INFO

Keywords:

Interfacial engineering
Copper foil
Current collector
Ultrafast lithium ion batteries
Surface modification

ABSTRACT

The interface engineering of anode electrodes in lithium-ion batteries (LIBs) is a key strategy in improving the Li-ion storage kinetics and interface stability to achieve outstanding ultrafast cycling capacities and cycling stabilities of LIBs. However, despite extensive research on the interfacial engineering of electrode materials, studies on the interface design between the electrode and current collector to improve the ultrafast cycling performance are rare. In this study, we designed a novel interface architecture for a fluorine-doped carbon quantum dot (F-CQD) interfacial layer on a stockade-like etched Cu foil via electrochemical modification and a spray coating process. The anode electrode assembled with the resultant Cu foil showed enhanced adhesion, high reaction kinetics, and excellent interface stability between the electrode and Cu foil due to the F-CQD interfacial layer on the stockade-like etched Cu foil, leading to an improved ultrafast cycling performance. Consequently, the novel architecture of a Cu foil having stockade-like etching patterns with an F-CQD interfacial layer showed an increased ultrafast cycling capacity of 82.9 mAh g⁻¹ and excellent ultrafast cycling stability of 94.1% after 500 cycles under ultrafast cycling conditions. These improved ultrafast cycling performances are due to the high contact area between the electrode and Cu foil, excellent reaction sites, and superb corrosion resistance.

1. Introduction

Owing to their superior energy density and long lifetime, lithium-ion batteries (LIBs) are extensively used in electrically powered devices such as military drones, electric vehicles, and power-assist suits where high gravimetric or volumetric energy densities are necessary [1,2]. However, despite utilization in various electrically-powered devices, they still have critical problems such as low mileages and poor cycling capacities with low stabilities under ultrafast charging conditions due to the unstable interface states (such as electrode//electrolyte, active material//additive material, and current collector//electrode) [3–5]. In particular, under ultrafast charging conditions, the peeling of the electrodes due to the volume expansion of the active materials, limited lithium/electron redox reaction kinetics, and rapid corrosion of the current collector are accelerated at the interface between the electrode and current collector, thus reducing the specific capacities and cycling stabilities of LIBs [6,7]. To overcome this limitation, interfacial engineering has been proposed as key strategies to improve the mechanical, chemical, electrical, and electrochemical stabilities of LIBs by the

geometric architecture of the interface and novel interface designs. From a material point of view, several studies have attempted to suppress the volume expansion and unstable interfacial reactions by adding a surface coating to the active material of the active materials (e.g., pitch coated graphite [8], Al₂O₃ coated amorphous Si, graphene coated Co₃O₄ [9], TiO₂ coated MoS₂ [10], and carbon coated CoS [11]) using interfacial engineering. However, despite the improvement in the volume expansion and interfacial stability of the active material, the peeling of the electrode from the current collector still poses a serious challenge. In recent years, several attempts have been made to prevent electrode peeling caused by corrosion of the current collector and to improve the ultrafast cycling performance through interfacial modification. This is a well-known strategy for stabilizing the interface between the electrode and current collector [12]. For example, Xiao et al. modified the surface of a Cu foil using the physical attack of steel balls and ultrasonication to increase the surface roughness [13]. Long et al. increased the surface roughness of a Cu foil using Cu micropowder decoration and powder sintering [14]. Cho et al. coated polydopamine on Cu foil to stabilize the interface [15]. However, despite these efforts, the degradation of the

* Corresponding author at: Program of Materials Science & Engineering, Convergence Institute of Biomedical Engineering and Biomaterials, Republic of Korea.
E-mail address: hjahn@seoultech.ac.kr (H.-J. Ahn).

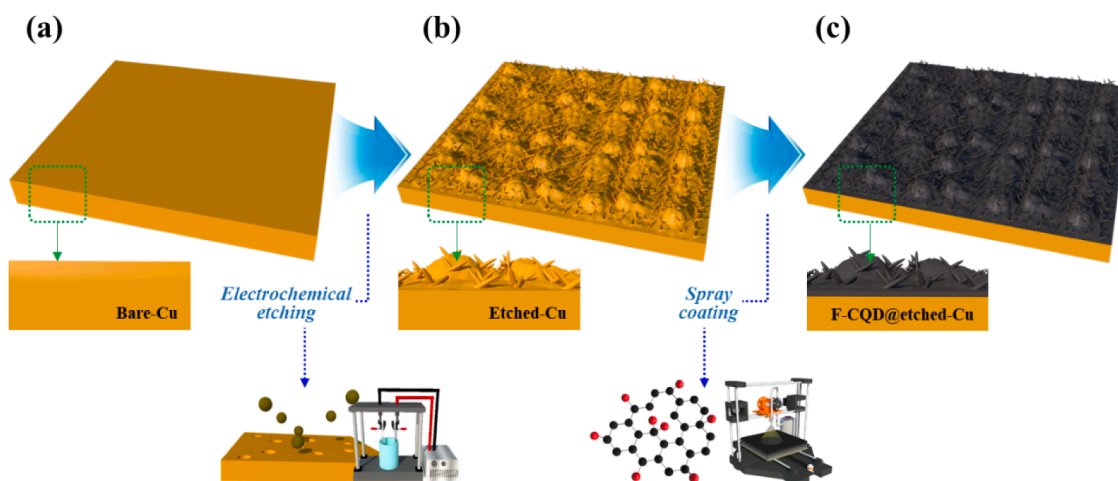


Fig. 1. Schematic illustration of electrochemical etching and direct spray coating of a bare Cu foil, b electrochemically etched Cu foil, and c F-CQD coated etched Cu foil to fabricate the F-CQD interfacial layer on stockade-like etched Cu foil.

electrode and low ultrafast cycling performance persisted. Therefore, to improve the cycling stability and ultrafast cycling performance, a novel interfacial engineering method that can enhance the interface between the electrode and current collector is required for ultrafast LIBs.

Here, we developed a novel interface architecture for a fluorine-doped carbon quantum dot (F-CQD) interfacial layer on a stockade-like etched Cu foil as a current collector for the anode electrode, and investigated the effect of the modified interface on the ultrafast cycling performances of ultrafast LIBs. The F-CQD showed excellent step coverage compared to other carbon materials such as graphene, carbon nanotubes, and graphite sheets. This was due to the small particle sizes (<10 nm) and high surface functional groups [16]. In addition, the F atoms doped in CQD can improve the ionic/electrical conductivity of the interfacial layer due to the C-F bond structure and the high electronegativity of F atoms [17]. Remarkably, this novel interface provided an enhanced interface between the electrode and current collector, which improved the adhesion area, redox reaction kinetics, and corrosion resistance. Consequently, under ultrafast cycling conditions (current density of 2000 mA g^{-1}), the F-CQD interfacial layer on stockade-like etched Cu foil exhibited an improved specific capacity and cycling stability compared those of the bare Cu foil.

2. Experimental section

2.1. Chemicals

Citric acid ($\text{HOC}(\text{COOH})(\text{CH}_2\text{COOH})_2$, 99.5%), urea (NH_2CONH_2 , 99.5%), trifluoroacetic acid ($\text{C}_2\text{HF}_3\text{O}_2$, 99%), N-methyl-2-pyrrolidone (NMP), and ammonium hydroxide solution (NH_4OH , 28%) were purchased from Sigma-Aldrich. Conventional Cu foil (thickness of 15 μm), and graphite powder (MesoCarbonMicroBead, MCNB), were purchased from MTI KOREA. All reagents were used as-received without further purifications.

2.2. Preparation of samples

2.2.1. Preparation of F-doped carbon quantum dot (F-CQD)

The F-CQDs were fabricated via a hydrothermal reaction and post-calcination. First, the CQDs were synthesized via a hydrothermal reaction. To synthesize the CQDs, 0.5 M citric acid and 0.45 M urea were dissolved in DI-water and stirred for 2 h. Then, the resulting solution was transferred into an 80 mL Teflon-lined stainless steel auto-clave and allowed to react at 180 $^\circ\text{C}$ for 6 h. Finally, the resulting solution was centrifuged 2 times at 10,000 rpm for 20 min and filtered using a tubular membrane with molecular weight cutoff of 12–14 kDa for 24 h to obtain

the CQD powder. The filtered CQD powder was dried in a conventional oven at 50 $^\circ\text{C}$. The F-CQD was synthesized by doping F into the CQD powder by post-calcination. To obtain the F-CQD, the as-prepared CQD and $\text{C}_2\text{HF}_3\text{O}_2$, which was used as the F doping source, were mixed in DI-water at a weight ratio of 1:1 and dried at 50 $^\circ\text{C}$ for 12 h in a dry oven. Post-calcination was then performed at 800 $^\circ\text{C}$ for 2 h in a high-purity nitrogen atmosphere (N_2 , 99.999%) using a tube-type furnace. To prepare the dispersion solution of F-CQD for spray coating, the F-CQD powder was dispersed in NMP and sonicated for 12 h.

2.2.2. Preparation of etched-Cu foil having stockade-like etching pattern and F-CQD@etched-Cu foil

The F-CQD@etched-Cu foil used as the current collector for the anode was fabricated using electrochemical etching and spray coating. To fabricate the stockade-like etched Cu foil, a bare Cu foil was electrochemically etched with 6 M NH_4OH using three electrode system, composed of a Pt wire (counter electrode), Ag/AgCl saturated in KCl (reference electrode), and Cu foil (working electrode) using a potentiostat/galvanostat (PGST302N by Eco Chemie, Netherlands). During the electrochemical etching of the Cu foil, the temperature and voltage were maintained at 25 $^\circ\text{C}$ and 1.2 V, respectively, for 300 s. Then, the etched Cu foil was washed several times with DI-water and dried at 50 $^\circ\text{C}$ for 5 h. The stockade-like etched Cu foil is hereafter referred to as etched-Cu. To form the F-CQD interfacial layer on the etched-Cu foil, the spray coating process was performed using the F-CQD suspension. During the spray coating process, the distance between the spray nozzle and the etched-Cu foil and temperature were fixed at 10 cm and 25 $^\circ\text{C}$, respectively. The spray-coated etched-Cu foil was dried at 50 $^\circ\text{C}$ for 10 h. The F-CQD-coated etched Cu foil is hereafter referred to as F-CQD@etched-Cu.

2.3. Material characterization

The surface morphology and surface roughness of the bare-Cu, etched-Cu, F-CQD@etched-Cu were investigated by field-emission scanning microscopy (FESEM, Hitachi S-4700) and atomic force microscopy (AFM, diDimension™ 3100). The crystal structures and chemical bonding states of the samples were determined using X-ray diffraction (XRD, Rigaku D/MAX2500V, used X-ray source of Cu K_α) and X-ray photoelectron spectroscopy (XPS, ESCALAB 250, used X-ray source of Al K_α). The electrical conductivities of the samples were determined using Hall measurements (Ecopia, HMS-3000). The elemental distribution of the electrodes at the initial and after the cycling test was analyzed by energy dispersive spectroscopy (EDS mapping).

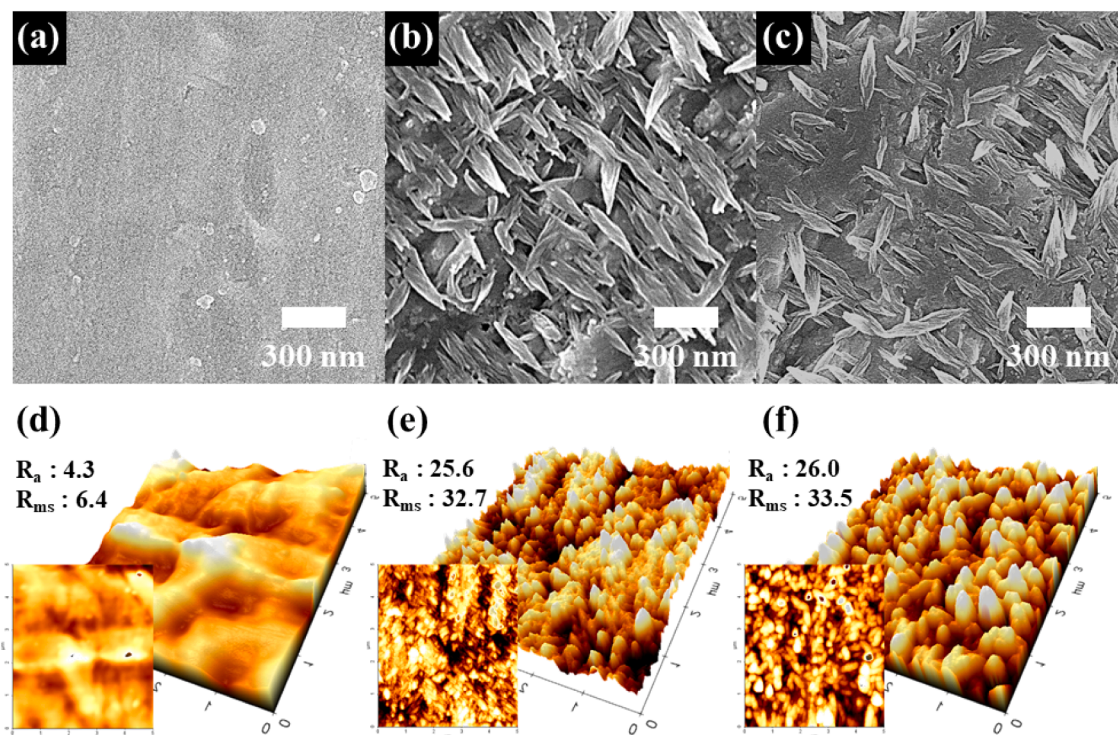


Fig. 2. Top-view FESEM images of (a) bare-Cu, (b) etched-Cu, and (c) F-CQD@etched-Cu. AFM images of (d) bare-Cu, (e) etched-Cu, and (f) F-CQD@etched-Cu, respectively.

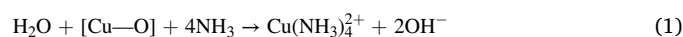
2.4. Electrochemical measurements

The electrochemical performances of the samples were analysed using coin-type half cells (CR2032, Hohsen Corp.), which is composed of an anode fabricated from bare-Cu, etched-Cu, and F-CQD@etched-Cu foil, a separator of porous polypropylene membrane (Celgard 2400), and an anode of Li metal (Honjo Chemical, 99.95%) in an electrolyte of 1.2 M LiPF₆ with additives of dimethyl carbonate (DMC) and ethylene carbonate (EC) (1:1 vol%). The anode electrode used with all samples was prepared using a mixed slurry consisting of 80 wt% graphite as the active material, 10 wt% polyvinylidene fluoride (PVDF) as the binder, and 10 wt% ketjen black as the conducting material in NMP as the solvent. Then, the slurry was applied as a coating on 20 μm of the as-prepared current collector using a doctor blade and dried at 100 °C for 10 h in a drying oven. The electrode density was fixed at 7.3 ± 0.1 mg cm⁻². The coin-type half cells were fabricated in an argon-filled glove box with water and oxygen concentrations of less than 5 ppm. To evaluate the electrochemical resistance and kinetics of all electrodes, electrochemical impedance spectroscopy (EIS) was performed in the frequency range of 10⁵ kHz and 10⁻² Hz at an AC voltage of 0.005 V. To investigate the electrochemical performances of all samples, cycling tests was performed using a battery cycle system (WonATech Corp., WMPG 3000) in the voltage range of 0.05–3.0 V (verse Li/Li⁺). Cycling stability test was observed up to 100 cycles at a current density of 100 mA g⁻¹. The rate performances were measured at current densities of 100, 300, 700, 1000, 1500, and 2000 mA g⁻¹. The ultrafast cycling properties were analyzed for up to 500 cycles at a current density of 2000 mA g⁻¹.

3. Results and discussion

Fig. 1 shows a schematic illustration of the electrochemical etching and spray coating processes of the Cu foil. The stockade-like interface on the Cu foil was formed by electrochemical etching using a potentiostat/galvanostat in an ammonia-based electrolyte, which was used as the

etchant. In general, Cu elements does not dissolve directly in ammonia (NH₄) solution without an oxidizing agent. However, the Cu components were ionized by the formation of chemical species such as Cu(NH₃)₄²⁺ and Cu(NH₃)₂²⁺, which were produced by the reaction of the adsorbed NH₄ and Cu on the surface of the Cu foil, in the voltage range of -0.2–0.6 V (vs. SHE) and pH range of 8–10 (Fig. S1). The electrochemical etching reaction of Cu in an ammonia-based electrolyte is as follows [18,19].



or



The electrochemically etched Cu foil with a stockade-like surface is an important factor for improving the adhesion between the electrode and Cu foil. The F-CQD interfacial layer was applied to the etched Cu foil by a spray coating process using the as-prepared F-CQD suspension. The F-CQD interfacial layer provided high electrical conductivity and excellent chemical stability to the Cu foil due to its unique quantum effect and C-F bonds [20,21]. In addition, from the Strong Metal-Support Interaction (SMSI) of view, F-CQD had strong interaction with the Cu foil due to high surface areas of functional groups, which can increase adhesion between F-CQD and the Cu foil [22,23]. In particular, the F-CQD interfacial layer effectively hindered the corrosion of the Cu foil from HF formed by decomposition of the electrolyte due to thier high step coverage. Therefore, the introduction of the F-CQD interfacial layer on the etched Cu foil was an effective strategy to increase the charge transfer and prevent the electrochemical corrosion of the Cu foil at the electrode-current collector interface during ultrafast cycling performance.

Fig. 2 shows the FESEM images of bare-Cu, etched-Cu, and F-CQD@etched-Cu. The bare-Cu foil had a smooth surface morphology (Fig. 2a), whereas the etched-Cu and F-CQD@etched-Cu had a rough surface morphologies with stockade-like etching patterns with a diameters of ~292.4–325.4 nm (aspect ratio of 4.72) (Fig. 2b) and a

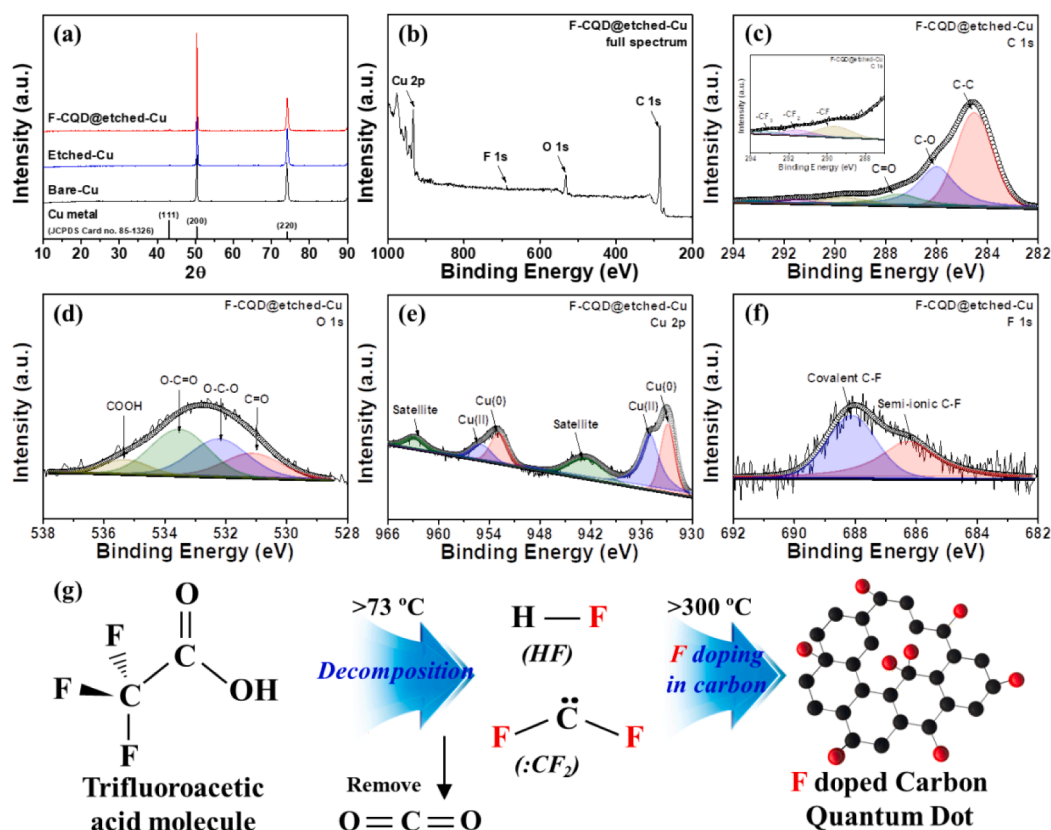


Fig. 3. (a) XRD data of all samples. (b) XPS full spectrum of F-CQD@etched Cu foil. XPS spectra obtained from (c) C 1s, (d) O 1s, (e) Cu 2p, and (f) F 1s of F-CQD@etched-Cu, respectively. (g) Schematic illustration of F doping process into carbon quantum dot.

diameter in the range ~ 293.5 – 326.9 nm (aspect ratio of 4.71) (Fig. 2c), respectively. In particular, the F-CQD interfacial layer of the F-CQD@etched-Cu was observed as nanodot shapes on the surface of the stockade-like etching patterns. However, it was difficult to distinguish the F-CQD interfacial layer on etched-Cu because of the complicated etching pattern of the F-CQD@etched-Cu foil. To confirm the presence of the F-CQD interfacial layer on the F-CQD@etched-Cu foil, we prepared an F-CQD coated Cu foil without etching (Fig. S2). The F-CQD interfacial layer showed an interconnected shape of nanoparticles with particle size in the range ~ 3.6 – 5.7 nm. The F-CQD interfacial layer acted as a passivation layer that can improve the ultrafast cycling performance of the F-CQD@etched-Cu by suppressing the corrosion of the Cu foil, thus providing an electron/ion transfer pathway [3]. To demonstrate the surface morphologies and roughnesses of all samples, AFM analysis was performed (Fig. 2d–f). The height roughness (R_a) and root-mean-square roughness (R_{ms}) values were ~ 4.3 nm and ~ 6.4 nm for the bare-Cu, ~ 25.6 nm and ~ 32.7 nm for the etched-Cu, and ~ 26.0 nm and ~ 33.5 nm for the F-CQD@etched-Cu, respectively. The increased surface roughness of the F-CQD@etched-Cu foil indicated that the stockade-like etching patterns and the F-CQD interfacial layer increased the interface contact area, thus enhancing the interfacial stability between the electrode and current collector. In addition, the bare-Cu foil showed a low surface roughness and a smooth surface morphology, whereas the F-CQD coated on the Cu foil without the etching process, indicated increased surface roughness due to the F-CQD interfacial layer on the Cu foil (Fig. S4). These results were consistent with the FESEM results.

To investigate the crystalline phases of the samples, XRD analysis were performed (Fig. 3a). The main characteristic diffraction peaks of bare-Cu, etched-Cu, and F-CQD@etched-Cu were observed at 43.6° , 50.8° , and 74.4° , which correspond to the (111), (200), and (220) planes of the Cu metal phase (space group of Fm-3m, JCPDS card No. 85-

1326), respectively [24]. Furthermore, only the diffraction peaks of Cu were observed in the XRD patterns of the bare-Cu, etched-Cu, and F-CQD@etched-Cu without the presence of other phases. The diffraction patterns of the F-CQDs in the F-CQD@etched-Cu were not clearly detected due to the relatively small amount of F-CQD. To confirm the crystal structure of the F-CQD, the F-CQD powder was analyzed by XRD. The diffraction peaks of the F-CQD were displayed at $\sim 23.9^\circ$ and $\sim 42.0^\circ$, which corresponded to the (002) and (100) planes of the F-CQD phase, respectively [25]. In addition, the sizes of the F-CQD particles were ~ 3.3 – 4.6 nm, calculated from $2\theta = 23.9^\circ$ and 42.0° using Bragg's equation (Fig. S5) [26]. Furthermore, to investigate the chemical bonding states of the F-CQD@etched-Cu, XPS analysis was performed (Fig. 3b–f). All the XPS spectra were calibrated using the C 1s binding energy of ~ 284.5 eV. In the XPS full scan spectrum of the F-CQD@etched-Cu (Fig. 3b), the spectra of C, F, O, and Cu elements were confirmed without the presence of other elements. The C 1s spectrum on F-CQD@etched-Cu (Fig. 3c) showed six signals at ~ 284.5 , ~ 286.0 , ~ 287.5 , ~ 289.8 , ~ 291.6 , and ~ 293.2 eV, which corresponded to the C–C, C–O, C=O, –CF, –CF₂, and –CF₃ bonds, respectively [27]. The C–F bonds were either covalent or semi-ionic bonds, and easily combined at defects in the carbon structure and functional groups containing oxygen (–O, –OH, –COOH, etc.) on the edge of carbon [3,28]. The O 1s spectrum of the F-CQD@etched-Cu (Fig. 3d) indicated at ~ 531.0 , ~ 532.1 , ~ 533.5 , and ~ 535.2 eV, which correspond to C=O, O–C–O, O–C=O, and COOH bonds, respectively [11,29]. The C–O bonds was formed at the F-CQD interfacial layer with oxygen-containing functional groups. The Cu 2p peak (Fig. 3e) of the F-CQD@etched-Cu showed two major peaks at ~ 932.8 eV for Cu 2p_{3/2} and ~ 952.8 eV for Cu 2p_{1/2}, indicating the metallic Cu state [30]. In addition, minor peaks were observed at ~ 933.8 eV for Cu 2p_{3/2} and ~ 953.8 eV for Cu 2p_{1/2}, which correspond to the Cu²⁺ state of either the CuO or CuO₂ phase. The F 1s spectrum of the F-CQD@etched-Cu (Fig. 3f) was located at ~ 686.1 and ~ 688.0 eV,

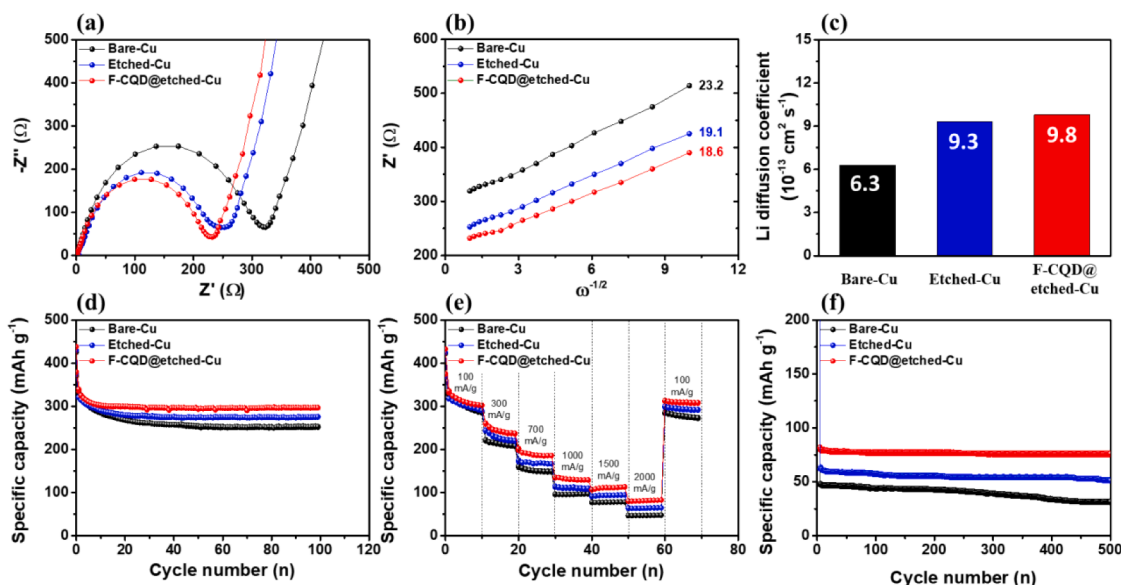


Fig. 4. (a) Nyquist plots of all sample electrodes. (b) Relationship between Z_{real} and $\omega^{-1/2}$ in the low frequency range of all electrodes. (c) Li^+ diffusion coefficients obtained from Warburg impedance of all sample electrodes. (d) Cycling test of all sample electrodes at a current density of 100 mA g^{-1} up to 100 cycles. (e) Rate-performance at a current density of 100 to 2000 mA g^{-1} . (f) Long-term ultrafast cycling test at 2000 mA g^{-1} up to 500 cycles.

which corresponded to semi-ionic and covalent C–F bonds, respectively [3]. The C–F bonding structure formed covalent bonds through semi-ionic bonds. In particular, as fluorine has a higher electronegativity (4.0) than carbon (2.5), the C–F bond provided a polarity/dipole moment, which improved the electron/ion transfer rate. Furthermore, C–F bonds expanded the carbon structure because of the increased distances between the carbon and fluorine atoms (0.17 nm for semi-ionic C–F and 0.14 nm for covalent C–F), which is a vertically bonded structure (Figs. S6 and S7) [3,31,32]. Fig. 3g shows the decomposition schematic of $\text{C}_2\text{HF}_3\text{O}_2$ and the doping process of F into the CQD during calcination. The decomposition equation of the $\text{C}_2\text{HF}_3\text{O}_2$ as the doping agent is as follows [33]:



First, $\text{C}_2\text{HF}_3\text{O}_2$ was decomposed to hydrogen fluoride (HF), vinylidene fluoride (CF_2), and carbon dioxide (CO_2) molecules at a temperature $> 73^\circ\text{C}$. Then, the F atoms in the HF and CF_2 acted as the dopants. These were doped into the CQDs during calcination at temperature $> 300^\circ\text{C}$. This confirmed that F-CQD can be synthesized using $\text{C}_2\text{HF}_3\text{O}_2$ [34].

To further demonstrate the charge transfer and Li ion diffusion kinetics in the fresh cells assembled with bare-Cu, etched-Cu, and F-CQD@etched-Cu, the EIS was measured. Fig. 4a displays the Nyquist plots of the samples in the frequency range between 10^5 kHz and 10^{-2} Hz at the open-circuit potential. The Nyquist plots consisted two regions: the semicircle (region I) at the low frequency part and the inclined line (region II) at the high frequency part (Fig. S8). Region I is composed of a double-layer capacitance (C_{dl}) which was related to the accumulated charge on the electrode surface with non-Faradaic reaction and charge transfer resistance (R_{ct}), which can be ascribed to the resistance to current flow with a Faradaic reaction [35,36]. Region II represented the diffusion impedance of the Li ions in the electrode (called the Warburg impedance) [35,36]. In the EIS data, the bare-Cu electrode displayed a large semicircle with poor Warburg impedance, which indicated low charge transfer kinetics resulting from the limited collection/provision sites and the poor contact area between the electrode and Cu foil. In contrast, the etched-Cu and F-CQD@etched-Cu electrodes showed smaller semicircle sizes than that of the bare-Cu electrode. The differences in the semicircle sizes of the samples was generally determined by the charge transfer resistance rather than the double-layer capacitances

because, the double-layer capacitances were similar in all the samples. Thus, the etched-Cu and F-CQD@etched-Cu electrodes exhibited low charge transfer resistance due to the enhanced charge collection and provision sites between the active materials and the Cu foil. In particular, the charge transfer resistance and Warburg impedance of the F-CQD@etched-Cu electrode were the lowest among the samples (Fig. 4b). The more efficient electrochemical kinetics of the F-CQD@etched-Cu were due to the introduced stockade-like etching patterns with the F-CQD interfacial layer. These etching patterns improved the high charge collection, provision sites, and fast charge transfer at the interface between the electrode and Cu foil. Fig. 4c shows the Li ion diffusion coefficient calculated from the Warburg impedance in the low-frequency region. The Li ion diffusion coefficient is calculated by the following equation [37,38]:

$$Z_{real} = R_e + R_{ct} + \sigma_w \omega^{-1/2} \quad (4)$$

$$D = (RT)^2 / 2(A n^2 C F^2 \sigma_w)^2 \quad (5)$$

where, R_e , R_{ct} , and σ_w are the bulk resistances ascribed to the overall resistance in the cell, charge transfer resistance, and Warburg impedance coefficient, respectively. R , T , A , n , C , and F are the gas constant, operating temperature, area of electrode, number of electrons, molar concentration of Li^+ , and Faraday constant, respectively. The Li ion diffusion coefficients, which were calculated using the Warburg impedance of bare-Cu, etched-Cu, and F-CQD@etched-Cu electrodes were 6.3×10^{-13} , 9.3×10^{-13} , and 9.8×10^{-13} , respectively. The Nyquist plots and Li ion diffusion coefficient results suggested that the stockade-like etching patterns and the F-CQD interfacial layer efficiently improved the electron transfer and Li ion diffusion rate during the ultrafast cycling performance. Thus, the increased electrochemical kinetics of the F-CQD@etched-Cu electrode can accelerated the Li ion storage rate under ultrafast cycling conditions.

To investigate the electrochemical performances of all samples, cycling stability tests were investigated in the voltage range of 0.05–3.0 V (verse Li/Li^+) at a current density of 100 mAh g^{-1} using the coin-type cells, as shown in Fig. 4d. The bare-Cu electrode exhibited a low specific capacity of 251.4 mAh g^{-1} with a poor capacity retention of 80.9% after 100 cycles. This was caused by the low interfacial stability due to the low contact area between the electrode and Cu foil. Conversely, the specific capacities of the etched-Cu and F-CQD@etched-Cu electrodes were

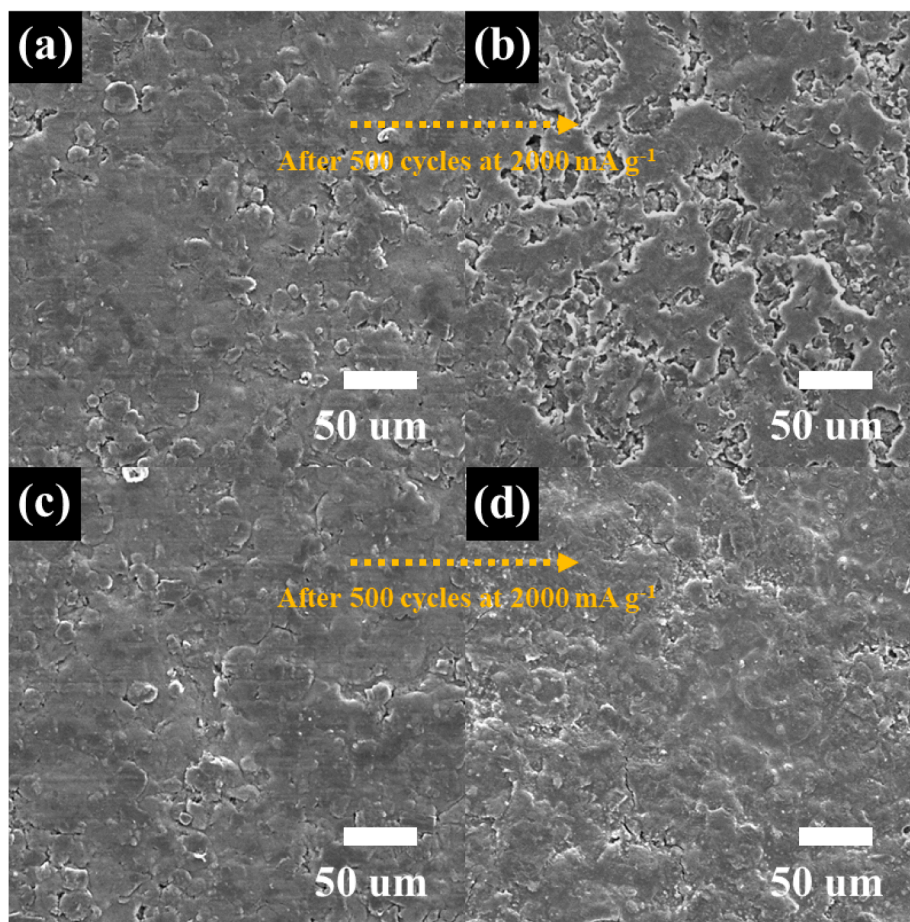


Fig. 5. Top-view FESEM images of (a), (c) initial state and (b), (d) after ultrafast cycling performance during 500 cycles at current density of 2000 mA g^{-1} obtained from bare-Cu and F-CQD@etched-Cu electrodes.

279.0 mAh g^{-1} with capacity retention of 89.2% and 297.3 mAh g^{-1} with a capacity retention of 94.3%, respectively, which are higher than those of the bare-Cu electrode. These results can be explained by the increased contact area and electron/ion transfer by the improved interface of the stockade-like etching patterns and the F-CQD interfacial layer. Fig. 4e shows the performance rates measured at current densities of 100, 300, 700, 1000, 1500, and 2000 mA g^{-1} . The specific capacity of the bare-Cu electrode decreased dramatically as the current density increased from 100 to 2000 mA g^{-1} . In contrast, the specific capacities of the etched-Cu and F-CQD@etched-Cu were 65.0 mAh g^{-1} and 82.9 mAh g^{-1} , respectively, even at a high current density of 2000 mA g^{-1} . In addition, compared to those of the CQDs without F doping coated on etched Cu foil, the specific capacity of F-CQD@etched-Cu was higher at 2000 mA g^{-1} (Fig. S9). Furthermore, the F-CQD@etched-Cu electrode showed outstanding ultrafast cycling performance compared to those of previously reported anode electrodes with graphite as the active material (Fig. S10) [39–46]. In particular, the specific capacity of the F-CQD@etched-Cu electrode was 2 times higher than that of the bare-Cu electrode, which had a low specific capacity decline rate at current densities in the range of 100 to 2000 mA g^{-1} (Fig. S11). To investigate the effects of the modified interface on the ultrafast cycling performance of the F-CQD@etched-Cu, we performed an ultrafast cycling test over a long period of 500 cycles, as shown in Fig. 4f. The bare-Cu electrode showed an extremely poor specific capacity of 31.1 mAh g^{-1} and a capacity retention of 64.4% after 500 cycles at a current density of 2000 mA g^{-1} . However, the F-CQD@etched-Cu electrode exhibited a significant improvement in the specific capacity (76.3 mAh g^{-1}) and capacity retention (94.1%) after 500 cycles at a current density of 2000 mA g^{-1} . A low current density (100 mA g^{-1}) was sufficient to cause the redox

reaction between lithium ions and electrons, resulting in no noticeably specific capacities (Fig. 4d). Conversely, the specific capacities of all samples at high current densities (2000 mA g^{-1}) were limited by the slow redox reaction kinetics of Li ions and electrons in the electrode. However, the F-CQD interfacial layer coated stockade-like etching patterns on Cu foil effectively improved the Li storage kinetics by increasing the number of electron collection/provision sites of electrons. This was because the specific capacity under ultrafast cycling conditions depended on the redox reaction kinetics of Li ions with electrons. Thus, the specific capacity of the F-CQD@etched-Cu electrode at a high current density was improved by increasing the redox reaction kinetics. Furthermore, to verify the effect of the interface modification, surface analysis was performed by disassembling the cells after the 500 cycles of the ultrafast cycling at a current density of 2000 mA g^{-1} .

Fig. 5 shows the surface state of the bare-Cu and F-CQD@etched-Cu electrodes after 500 cycles at a current density of 2000 mA g^{-1} . Before the cycling test, the bare-Cu and F-CQD@etched-Cu electrodes indicated a smooth surface state without electrode breakage (Fig. 5a and c). However, after 500 cycles under ultrafast cycling conditions, the surface of the bare-Cu electrode was seriously damaged due to electrode decomposition caused by volume expansion and the peeling of the electrode (Fig. 5b and Fig. S12a) [3]. By contrast, the F-CQD@etched-Cu electrode displayed a smooth surface structure similar to the initial surface state even after the ultrafast cycling test (Fig. 5d and Fig. S12b) owing to the improved interfacial stability by outstanding contact area and corrosion resistance between stockade-like etching patterns and the F-CQD interfacial layer. The by-product of the electrolyte (such as HF) severely corroded the Cu foil under ultrafast cycling conditions, thus decreasing the specific capacity. Then, the dissolved Cu components

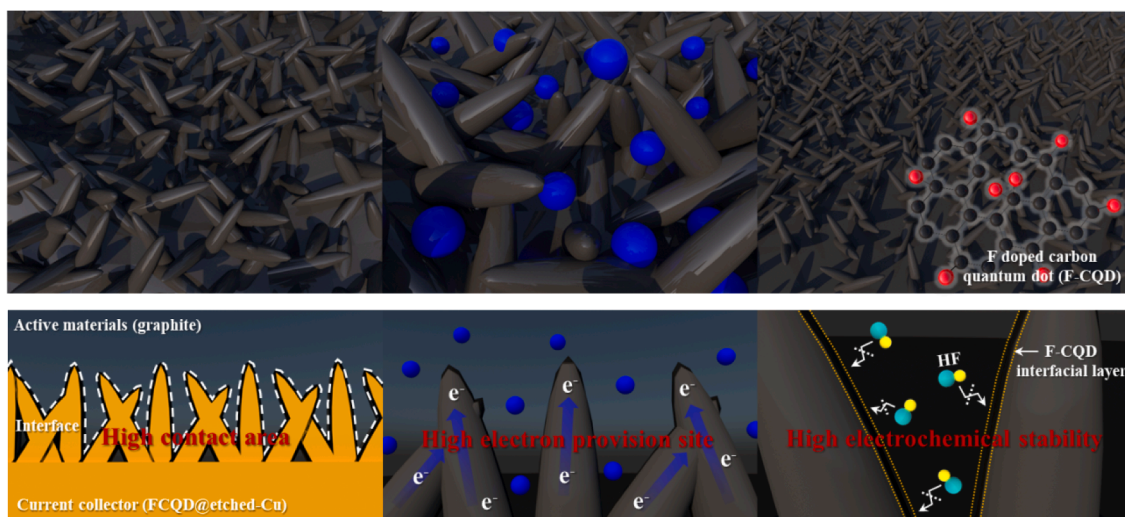


Fig. 6. Schematic illustration of the three main effects on the F-CQD@etched-Cu electrode for improving ultrafast cycling.

migrated and precipitated on the electrode surface [47,48]. In the EDS results, the Cu components on the surface of the bare-Cu electrode significantly increased from 0.4 to 5.8 at.%, while the Cu components of the F-CQD@etched-Cu electrode increased slightly from 0.4 to 1.7 at.% (Fig. S13 and Table S1). In addition, the enhanced interfacial stability of the F-CQD@etched-Cu electrode also maintained the electrical/electrochemical resistance of the cell compared to that of the bare-Cu electrode (Fig. S14). The electrode underwent severe capacity degradation under ultrafast cycling conditions because of the low contact area and poor electrochemical stability of the interface between the electrode and Cu foil, which is attributed to the accelerated volume expansion and limited ion/electron transfer rate. However, the F-CQD@etched-Cu electrode displayed a significantly increased ultrafast cycling performance, resulting from the improved contact area and enhanced electrochemical stability due to the introduction of the stockade-like etching patterns and the F-CQD interfacial layer.

Thus, in this study, the facilitated ultrafast cycling performance at a current density of 2000 mA g^{-1} of the F-CQD@etched-Cu electrode was achieved by introducing a novel F-CQD interfacial layer on stockade-like etched Cu foil. The enhancement factor of the ultrafast cycling performance can be ascribed to the three main effects of the F-CQD interfacial layer on the stockade-like etched Cu foil (Fig. 6): (I) the stockade-like etching patterns on Cu foil improved the contact area between the electrode and Cu foil, thus enhancing the cycling stability (Fig. 6a); (II) the increased collection/provision sites of the current collector significantly enhanced the ultrafast cycling capacity by facilitating the fast reaction of Li ions with electrons (Fig. 6b); and (III) the introduced F-CQD interfacial layer effectively prevented corrosion of the Cu foil by the by-products in the electrolyte, thus leading to an increased ultrafast cycling stability (Fig. 6c).

4. Conclusion

In this study, we proposed a novel strategy for engineering of the interface between the electrode and current collector in ultrafast LIBs. This was achieved by applying a coating of an F-CQD interfacial layer onto stockade-like etched Cu foil. This offered synergistic effects which improved the ultrafast cycling performance and electrochemical kinetics. The F-CQD@etched-Cu electrode exhibited a stockade-like etching pattern in the size range of 293.5–326.9 nm (aspect ratio of 4.71). In addition, this novel structure showed an improved Li ion diffusion coefficient ($9.8 \times 10^{-13} \text{ cm}^2 \text{ s}^{-1}$). Furthermore, when the F-CQD@etched-Cu was used as the current collector in the anode for the LIB, the cycling stability was 297.3 mAh g^{-1} with a capacity retention of

94.3% after 100 cycles at 100 mA g^{-1} . Furthermore, at an ultrafast cycling condition of 2000 mA g^{-1} , the ultrafast cycling capacity of the F-CQD@etched-Cu electrode was 2 times higher than that of the bare-Cu electrode. In particular, the ultrafast cycling stability of the F-CQD@etched-Cu electrode was 94.1%, which is 1.5 times higher than that of the bare-Cu electrode. These results could be attributed to the following multifunctional effects of the F-CQD interfacial layer on the stockade-like etched Cu foil. First, the improved cycling stability could be attributed to the increased contact area between the electrode and Cu foil due to the formation of stockade-like etching patterns on the Cu foil. Second, the outstanding ultrafast cycling capacity was due to the increased number of collection/provision sites, which increased the reaction of electrons and Li ions. Third, the introduced F-CQD interfacial layer significantly prevented the corrosion of the Cu foil, thus enhancing the ultrafast cycling stability. Therefore, the introduction of the F-CQD interfacial layer on stockade-like etched Cu foil was an effective strategy for boosting the ultrafast cycling performances and electrochemical kinetics of LIBs.

Declaration of Competing Interest

The authors declare that they have no known competing financial interests or personal relationships that could have appeared to influence the work reported in this paper.

Acknowledgments

This work was supported by the Technology Innovation Program (10080656, Development of ceramic/carbon convergence and integration anode material for 10 C fast charging Lithium ion battery) funded by the Ministry of Trade, Industry & Energy (MOTIE, Korea)

Appendix A. Supplementary data

Supplementary data to this article can be found online at <https://doi.org/10.1016/j.cej.2020.127563>.

References

- [1] J. Yuan, J. Zhu, R. Wang, Y. Deng, S. Zhang, C. Yao, Y. Li, X. Li, C. Xu, 3D few-layered MoS_2 /graphene hybrid aerogels on carbon fiber papers: a free-standing electrode for high-performance lithium/sodium-ion batteries, *Chem. Eng. J.* 398 (2020) 125592, <https://doi.org/10.1016/j.cej.2020.125592>.
- [2] L. Yang, L. Yang, G. Xu, Q. Feng, Y. Li, E. Zhao, J. Ma, S. Fan, X. Li, Separation and recovery of carbon powder in anodes from spent lithium-ion batteries to synthesize

- graphene, *Sci. Rep.* 9 (823) (2019) 1–7, <https://doi.org/10.1038/s41598-019-46393-4>.
- [3] D.-Y. Shin, H.-J. Ahn, Interfacial engineering of a heteroatom-doped graphene layer on patterned aluminum foil for ultrafast lithium storage kinetics, *ACS Appl. Mater. Interfaces* 12 (16) (2020) 19210–19217, <https://doi.org/10.1021/acscami.0c01774.s001>.
- [4] D.-Y. Shin, B.-R. Koo, H.-J. Ahn, Lithium storage kinetics of highly conductive F-doped SnO₂ interfacial layer on lithium manganese oxide surface, *Appl. Surf. Sci.* 499 (144057) (2020) 1–9, <https://doi.org/10.1016/j.apsusc.2019.144057>.
- [5] H. Wang, H. Jiang, Y. Hu, Z. Deng, C. Li, Interface engineering of few-layered MoS₂ nanosheets with ultrafine TiO₂ nanoparticles for ultrastable Li-ion batteries, *Chem. Eng. J.* 345 (2018) 320–326, <https://doi.org/10.1016/j.cej.2018.03.166>.
- [6] D.-Y. Shin, D.-H. Park, H.-J. Ahn, Interface modification of an Al current collector for ultrafast lithium-ion batteries, *Appl. Surf. Sci.* 475 (2019) 519–523, <https://doi.org/10.1016/j.apsusc.2019.01.016>.
- [7] X. Li, S. Deng, M.N. Banis, K. Doyle-Davis, D. Zhang, T. Zhang, J. Yang, R. Divigalpitiya, F. Brandys, R. Li, X. Sun, Suppressing corrosion of aluminum foils via highly conductive graphene-like carbon coating in high-performance lithium-based batteries, *ACS Appl. Mater. Interfaces* 11 (36) (2019) 32826–32832, <https://doi.org/10.1021/acscami.9b06442.s001>.
- [8] Y.-J. Han, J. Kim, J.-S. Yeo, J.C. An, I.-P. Hong, K. Nakabayashi, J. Miyawaki, J.-D. Jung, S.-H. Yoon, Coating of graphite anode with coal tar pitch as an effective precursor for enhancing the rate performance in Li-ion batteries: effects of composition and softening points of coal tar pitch, *Carbon* 94 (2015) 432–438, <https://doi.org/10.1016/j.carbon.2015.07.030>.
- [9] Y.u. He, X. Yu, Y. Wang, H. Li, X. Huang, Alumina-coated patterned amorphous silicon as the anode for a lithium-ion battery with high coulombic efficiency, *Adv. Mater.* 23 (42) (2011) 4938–4941, <https://doi.org/10.1002/adma.201102568>.
- [10] X. Yang, K. Fan, Y. Zhu, J. Shen, X. Jiang, P. Zhao, S. Luan, C. Li, Electric papers of graphene-coated Co 3 O 4 fibers for high-performance lithium-ion batteries, *ACS Appl. Mater. Interfaces* 5 (3) (2013) 997–1002, <https://doi.org/10.1021/am302685t>.
- [11] D.-Y. Shin, H.-G. Jo, H.-J. Ahn, Accelerating lithium storage capability of cobalt sulfide encapsulated within anion dual-doped mesoporous carbon nanofibers, *Appl. Surf. Sci.* 527, 146895 (2020) 1–9, <https://doi.org/10.1016/j.apsusc.2020.146895>.
- [12] C. Zhang, R. Lyu, W. Lv, H. Li, W. Jiang, J. Li, S. Gu, G. Zhou, Z. Huang, Y. Zhang, J. Wu, Q.-H. Yang, F. Kang, A lightweight 3D Cu nanowire network with phosphidation gradient as current collector for high-density nucleation and stable deposition of lithium, *Adv. Mater.* 31 (48) (2019) 1904991, <https://doi.org/10.1002/adma.201904991>.
- [13] Z. Xiao, J. Chen, J. Liu, T. Liang, Y. Xu, C. Zhu, S. Zhong, Microcrystalline copper foil as a high performance collector for lithium-ion batteries, *J. Power Sources* 438 (226973) (2019) 1–10, <https://doi.org/10.1016/j.jpowsour.2019.226973>.
- [14] J. Long, H. Liu, Y. Xie, W. Tang, T. Fu, Y. Tang, L. Lu, X. Ding, X. Tang, Three-dimensional copper foil-powder sintering current collector for a silicon-based anode lithium-ion battery, *Materials* 11 (1338) (2018) 1–7, <https://doi.org/10.3390/ma11081338>.
- [15] I. Sho, S. Gong, D. Song, Y.-G. Lee, M.-H. Ryou, Y.M. Lee, Mussel-inspired polydopamine-treated copper foil as a current collector for high-performance silicon anodes, *Sci. Rep.* 6 (30945) (2016) 1–9, <https://doi.org/10.1038/srep30945>.
- [16] I.-A. Baragau, Z. Lu, N.P. Power, D.J. Morgan, J. Bowen, P. Diaz, S. Kellici, Continuous hydrothermal flow synthesis of S-functionalised carbon quantum dots for enhanced oil recovery, *Chem. Eng. J.* 405 (2021) 126631, <https://doi.org/10.1016/j.cej.2020.126631>.
- [17] C. Liang, H.-Y. Niu, H. Guo, C.-G. Niu, Y.-Y. Yang, H.-Y. Liu, W.-W. Tang, H.-P. Feng, Efficient photocatalytic nitrogen fixation to ammonia over bismuth monoxide quantum dots-modified defective ultrathin graphitic carbon nitride, *Chem. Eng. J.* 406 (2021) 126868, <https://doi.org/10.1016/j.cej.2020.126868>.
- [18] Z. Sun, H. Cao, P. Venkatesan, W. Jin, Y. Xiao, J. Sietsma, Y. Yang, Electrochemistry during efficient copper recovery from complex electronic waste using ammonia based solutions, *Front. Chem. Sci. Eng.* 11 (3) (2017) 308–316, <https://doi.org/10.1007/s11705-016-1587-x>.
- [19] H.-H. Deng, K.-L. Li, Q.-Q. Zhuang, H.-P. Peng, Q.-Q. Zhuang, A.-L. Liu, X.-H. Xia, W. Chen, An ammonia-based etchant for attaining copper nanoclusters with green fluorescence emission, *Nanoscale* 10 (14) (2018) 6467–6473, <https://doi.org/10.1039/C7NR09449C>.
- [20] G. Zuo, A. Xie, J. Li, T. Su, X. Pan, W. Dong, Large emission red-shift of carbon dots by fluorine doping and their applications for red cell imaging and sensitive intracellular Ag⁺ detection, *J. Phys. Chem. C* 121 (2017) 26558–26565, <https://doi.org/10.1021/acs.jpcc.7b10179>.
- [21] R.u. Wang, K.-Q. Lu, Z.-R. Tang, Y.-J. Xu, Recent progress in carbon quantum dots: synthesis, properties and applications in photocatalysis, *J. Mater. Chem. A* 5 (8) (2017) 3717–3734, <https://doi.org/10.1039/C6TA08660H>.
- [22] Z. Li, C. Wang, X. Chen, X. Wang, X. Li, Y. Yamauchi, X. Xu, J. Wang, C. Lin, D. Luo, X. Wang, X.S. Zhao, MoO₃ nanoparticles anchored on N-doped porous carbon as Li-ion battery electrode, *Chem. Eng. J.* 381 (2020) 122588, <https://doi.org/10.1016/j.cej.2019.122588>.
- [23] C. Liu, C. Wang, X. Meng, X. Li, Q. Qing, X. Wang, R. Xue, Q. Yu, J. Yang, K. Wang, X. Zhao, W. Chen, Z.-A. Qiao, X.S. Zhao, Tungsten nitride nanoparticles anchored on porous borocarbonitride as high-rate anode for lithium ion batteries, *Chem. Eng. J.* 399 (2020) 125705, <https://doi.org/10.1016/j.cej.2020.125705>.
- [24] S. Ammara, S. Shamaila, R. Sharif, S. Ghani, N. Zafar, Uniform and homogeneous growth of copper nanoparticles on electrophoretically deposited carbon nanotubes electrode for nonenzymatic glucose sensor, *Acta Metall. Sin. (Engl. Lett.)* 29 (10) (2016) 889–894, <https://doi.org/10.1007/s40195-016-0476-0>.
- [25] N.R. Devi, T.H.V. Kumar, A.K. Sundramoorthy, Electrochemically exfoliated carbon quantum dots modified electrodes for detection of dopamine neurotransmitter, *J. Electrochem. Soc.* 165 (12) (2018) G3112–G3119, <https://doi.org/10.1149/2.0191812jes>.
- [26] T.N.J.I. Edison, R. Atchudan, M.G. Sethuraman, J.-J. Shim, Y.R. Lee, Microwave assisted green synthesis of fluorescent N-doped carbon dots: cytotoxicity and bio-imaging application, *J. Photochem. Photobiol. B-Biol.* 161 (2016) 154–161, <https://doi.org/10.1016/j.jphotobiol.2016.05.017>.
- [27] D.-Y. Sin, I.-K. Park, H.-J. Ahn, Enhanced electrochemical performance of phosphorus incorporated carbon nanofibers by the spin-on dopant method, *RSC Adv.* 6 (63) (2016) 58823–58830, <https://doi.org/10.1039/C6RA06782D>.
- [28] B. Gupta, N. Kumar, K. Panda, V. Kanan, S. Joshi, I.V. Fisher, Role of oxygen functional groups in reduced graphene oxide for lubrication, *Sci. Rep.* 7 (45030) (2017) 1–14, <https://doi.org/10.1038/srep45030>.
- [29] D.-Y. Shin, K.-W. Sung, H.-J. Ahn, Synergistic effect of heteroatom-doped activated carbon for ultrafast charge storage kinetics, *Appl. Surf. Sci.* 478 (2019) 499–504, <https://doi.org/10.1016/j.apsusc.2019.01.186>.
- [30] H. Nie, L. Fu, J. Zhu, W. Yang, D. Li, L. Zhou, Excellent tribological properties of low reduced graphene oxide content copper composite by using a one-step reduction molecular-level mixing process, *Materials* 11 (600) (2018) 1–14, <https://doi.org/10.3390/ma11040600>.
- [31] T. Gong, R. Qi, X. Liu, H. Li, Y. Zhang, N. F-codoped microporous carbon nanofibers as efficient metal-free electrocatalysts for ORR, *Nano-Micro Lett.* 11 (9) (2019) 1–11, <https://doi.org/10.1007/s40820-019-0240-x>.
- [32] P. Wang, B. Qiao, Y. Du, Y. Li, X. Zhou, Z. Dai, J. Bao, Fluorine-doped carbon particles derived from lotus petioles as high-performance anode materials for sodium-ion batteries, *J. Phys. Chem. C* 119 (37) (2015) 21336–21344, <https://doi.org/10.1021/acs.jpcc.5b05443>.
- [33] H. Hori, Y. Takano, K. Koike, K. Takeuchi, H. Einaga, Decomposition of environmentally persistent trifluoroacetic acid to fluoride ions by a homogeneous photocatalyst in water, *Environ. Sci. Technol.* 37 (2) (2003) 418–422, <https://doi.org/10.1021/es025783y>.
- [34] S. Huang, Y. Li, Y. Feng, H. An, P. Long, C. Qin, W. Feng, Nitrogen and fluorine codoped graphene as a high-performance anode material for lithium-ion batteries, *J. Mater. Chem. A* 3 (46) (2015) 23095–23105, <https://doi.org/10.1039/C5TA06012E>.
- [35] Y. Zhong, B. Li, S. Li, S. Xu, Z. Pan, Q. Huang, L. Xing, C. Wang, W. Li, Bi nanoparticles anchored in N-doped porous carbon as anode of high energy density lithium ion battery, *Nano-Micro Lett.* 10 (56) (2018) 1–14, <https://doi.org/10.1007/s40820-018-0209-1>.
- [36] J. Xie, L. Liu, J. Xia, Y. Zhang, M. Li, Y. Ouyang, S. Nie, X. Wang, Template-free synthesis of Sb₂S₃ hollow microspheres as anode materials for lithium-ion and sodium-ion batteries, *Nano-Micro Lett.* 10 (12) (2018) 1–12, <https://doi.org/10.1007/s40820-017-0165-1>.
- [37] B.-R. Koo, K.-W. Sung, H.-J. Ahn, Boosting ultrafast lithium storage capability of hierarchical core/shell constructed carbon nanofiber/3D interconnected hybrid network with nanocarbon and FTO nanoparticle heterostructures, *Adv. Funct. Mater.* 30 (32) (2020) 2001863, <https://doi.org/10.1002/adfm.202001863>.
- [38] G.-H. An, D.-Y. Lee, H.-J. Ahn, Tunneled mesoporous carbon nanofibers with embedded ZnO nanoparticles for ultrafast lithium storage, *ACS Appl. Mater. Interfaces* 9 (14) (2017) 12478–12485, <https://doi.org/10.1021/acsami.7b01286.s001>.
- [39] W. Yuan, J. Luo, Z. Yan, Z. Tan, Y. Tang, High-performance CuO/Cu composite current collectors with array-pattern porous structures for lithium-ion batteries, *Electrochim. Acta* 226 (2017) 89–97, <https://doi.org/10.1016/j.electacta.2016.12.139>.
- [40] Z. Ma, Y. Zhuang, Y. Deng, X. Song, X. Zuo, X. Xiao, J. Nan, From spent graphite to amorphous sp² + sp³ carbon-coated sp² graphite for high-performance lithium ion batteries, *J. Power Sources* 376 (2018) 91–99, <https://doi.org/10.1016/j.jpowsour.2017.11.038>.
- [41] W. Yuan, B. Pan, Z. Qiu, Z. Peng, Y. Ye, Y. Huang, H. Huang, Y. Tang, Using orthogonal ploughing/extrusion to fabricate three-dimensional on-chip-structured current collector for lithium-ion batteries, *ACS Sustain. Chem. Eng.* 7 (15) (2019) 12910–12919, <https://doi.org/10.1021/acscuschemeng.9b01899.s001>.
- [42] J. Billaud, F. Bouville, T. Magrini, C. Villeveuille, A.R. Studart, Magnetically aligned graphite electrodes for high-rate performance Li-ion batteries, *Nat. Energy* 1 (2838) (2016) 1–6, <https://doi.org/10.1038/NENERGY.2016.97>.
- [43] Y. Yang, S. Song, S. Lei, W. Sung, H. Hou, F. Jiang, X. Ji, W. Zhao, Y. Hu, A process for combination of recycling lithium and regenerating graphite from spent lithium-ion battery, *Waste Manage.* 85 (2019) 529–537, <https://doi.org/10.1016/j.wasman.2019.01.008>.
- [44] Y. Yan, C. Li, C. Liu, Z. Mutlu, B. Dong, J. Liu, C.S. Ozkan, M. Ozkan, Bundled and dispersed carbon nanotube assemblies on graphite superstructures as free-standing lithium-ion battery anodes, *Carbon* 142 (2019) 238–244, <https://doi.org/10.1016/j.carbon.2018.10.044>.
- [45] Q. Cheng, Y. Zhang, Multi-channel graphite for high-rate lithium ion battery, *J. Electrochem. Soc.* 165 (5) (2018) A1104–A1109, <https://doi.org/10.1149/2.1171805jes>.
- [46] Z. Tai, Y. Liu, Q. Zhang, T. Zhou, Z. Guo, H.K. Liu, S.X. Dou, Ultra-light and flexible pencil-trace anode for high performance potassium-ion and lithium-ion batteries,

- Green Energy Environ. 2 (3) (2017) 278–284, <https://doi.org/10.1016/j.gee.2017.04.002>.
- [47] Q. Li, S. Zhu, Y. Lu, 3D porous Cu current collector/Li-metal composite anode for stable lithium-metal batteries, *Adv. Funct. Mater.* 27 (1606422) (2017) 1–8, <https://doi.org/10.1002/adfm.201606422>.
- [48] L.-L. Lu, J. Ge, J.-N. Yang, S.-M. Chen, H.-B. Yao, F. Zhou, S.-H. Yu, Free-standing copper nanowire network current collector for improving lithium anode performance, *Nano Lett.* 16 (7) (2016) 4431–4437, <https://doi.org/10.1021/acs.nanolett.6b01581.s001>.